Journal of Petroleum Science and Engineering 213 (2022) 110375

Contents lists available at ScienceDirect

Journal of Petroleum Science and Engineering

journal homepage: www.elsevier.com/locate/petrol

Physical and Mechanical characteristic relationships of Late-Cretaceous to Eocene reservoir rocks in the Maui, Maari and Manaia Fields, New Zealand

Sophie Hill [a], Marlène C. Villeneuve [a,*], David McNamara [b,1]

[a] Department of Geological Sciences, University of Canterbury, Christchurch, New Zealand
[b] GNS Science, Avalon, New Zealand

ARTICLE INFO

Keywords:
Rock strength
Mohr-coulomb
Hoek-Brown
Porosity
Grain size
Maui Maari field

ABSTRACT

Constraint on the rock strength parameters within the subsurface is a fundamental requirement for accurate geomechanical modelling of aspects of reservoir stability and regional scale basin interactions. Insufficient rock strength data for offshore lithologies within the Taranaki Basin leads to a dependence on uncalibrated, empirical relationships applied in conjunction with wireline measurements for rock strength predictions. Use of these uncalibrated empirical relationships can lead to unreliable strength estimates, which reduces the confidence in geomechanical modelling and the subsequent solutions for the region.

We conducted uniaxial and triaxial experiments on cores from offshore Taranaki reservoir rocks from 2000 to 4000 m depth to develop the first, calibrated, empirical rock strength relationships for reservoir rocks of the Taranaki Basin, using both grain size and porosity as input parameters. We show that grain size and porosity can be used as predictive tools for determining Hoek-Brown and Mohr-Coulomb failure criterion parameters for petroleum geomechanics. As mean grain diameter and porosity are the dominant control on rock strength, we infer that rock strength parameters within the Taranaki Basin will follow a similar spatial distribution as the reservoir sandstone facies, which are dominantly defined by grain size.

We also show that the empirical relationships we developed with this dataset can be locally calibrated for other parts of the Taranaki basin, and indeed for other sandstones, such as the Buntsandstein from the Rhine Graben, France. Finally, we provide an approach by which grain size (+/− porosity) can be used to approximate the input parameters for the Hoek-Brown failure criterion in the absence of laboratory experiments. We propose, therefore, that the empirical relationships presented herein can be used to link facies descriptions with first-order estimates of mechanical properties at the basin scale.

1. Introduction

Compressive rock strength is an important input parameter utilized in geomechanical assessment, to model regional scale basin interactions with the contemporary stress field and to assess formation stability (Holt et al., 1989; Chang et al., 2006; Massiot et al., 2019). For geomechanical characterisation of a region, the uniaxial compressive strength (UCS) of an interval is a key component used for in-situ stress field calculations. In drilling assessment, a linear poro-elasticity stress model in conjunction with a failure criterion e.g. Hoek-Brown or Mohr Coulomb, is used to assess rock strength at depth and determine the optimum mud pressure and drilling direction required for a stable wellbore (Zhang et al., 2010; Gholami et al., 2014). Knowledge of the compressive rock strength is required to accurately address reservoir geomechanical problems such as borehole breakouts and sand production (Zhang et al., 1998).

The southern Taranaki Basin represents a region of extensive petroleum development in New Zealand, with many exploratory boreholes. Geomechanical studies previously undertaken in the Taranaki region are limited to wellbore stability by industry, which rely on the determination of rock strength parameters of the formations being drilled through (OMV New Zealand Limited, 1998–2006, Shell Todd Oil Services Ltd, 2001, Shell Todd Oil Services Ltd, 2002, New Zealand Overseas Petroleum Limited, 2005, Swift Energy, 2007a, Swift Energy, 2007b, Todd Energy, 2010). Given the lack of a geomechanical properties database for reference, this practice can lead to error considering

* Corresponding author. Chair of Subsurface Engineering, Montanuniversität Leoben, Erzherhog Johannstraße 3/III, 8700, Leoben, Austria.
E-mail address: marlene.villeneuve@unileoben.ac.at (M.C. Villeneuve).
[1] Present address: Department of Earth, Ocean and Ecological Sciences, University of Liverpool, Liverpool, UK.

https://doi.org/10.1016/j.petrol.2022.110375
Received 22 October 2021; Received in revised form 24 February 2022; Accepted 3 March 2022
Available online 4 March 2022

wellbore design and drilling in the Taranaki basin resulting in potential well failure with potential economic and environmental consequences. This highlights the need for increased laboratory testing to better constrain the rock strength parameters across the basin.

In cases where the availability of laboratory data is limited, rock strength in the subsurface is often estimated with empirical relationships utilizing other physical properties measured from wireline logging e.g. compressional wave velocity and/or porosity (Moos et al., 2001; Chang et al., 2006; Fjaer et al., 2008). The most common parameters utilized in these empirical strength relations include porosity (n), and

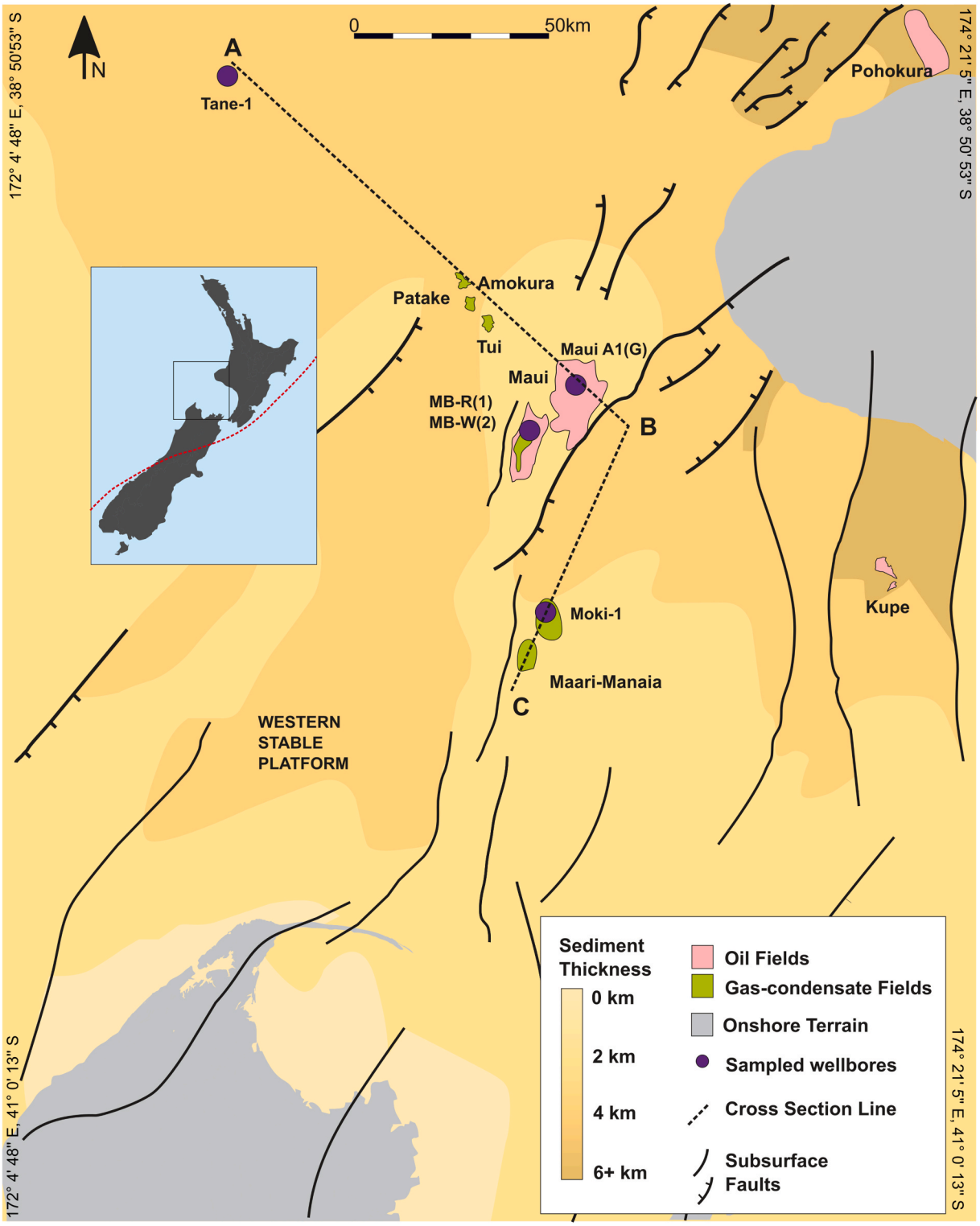

Fig. 1. Regional map of southern Taranaki Basin with structural controlling faults separating the Western Stable Platform and Eastern Mobile Belt. Petroleum fields and wellbores referenced in text are indicated, and cross section line for Fig. 4 (ABC′) is delineated. The dashed red line in the inset highlights the plate boundary between the Australian and Pacific plates. Modified from New Zealand Petroleum & minerals (2014). (For interpretation of the references to colour in this figure legend, the reader is referred to the Web version of this article.)

compressional wave velocity (V_p) or compressional slowness (DTC). However, without calibration of the empirical strength relations between these parameters and the actual measured strength of the geological units of a resource, the rock strength predictions may be inaccurate and thus unreliable for geomechanical modelling solutions. In addition, empirical rock strength relationships rarely consider petrophysical properties such as grain size as input parameters (Ulusay et al., 1994; Atapour and Mortazavi, 2018), despite grain size providing a dominant control on rock strength parameters (Fredrich et al., 1990; Hoek et al., 1992; Wong et al., 1997; Carbillet et al., 2021). In addition, numerical modelling has been used to explore the impact of grain size on strength under conditions that can be more easily controlled than when conducting laboratory experiments on natural samples. Peng et al. (2017) and Xu et al. (2020), for example showed that increasing grain size heterogeneity decreases strength, while Yu et al. (2018) showed that larger grains induce higher local stress concentrations, thereby reducing strength. This points to grain size as a suitable target for developing empirical relationships.

Sandstone reservoirs occur under confinement stress conditions and are typically fluid saturated, and the in-situ strength will depend on the impact of the resulting effective confining stress and saturation. It has been well established that confinement stress increases rock strength, and is the basis for well-known failure criteria such as Mohr-Coulomb (Labuz and Zang, 2012) and Hoek-Brown (Eberhardt, 2012), whereas water saturation decreases sandstone strength (e.g. Baud et al., 2000; Duda and Renner, 2013; Wasantha and Ranjith, 2014; Tang et al., 2018). Conducting uniaxial and triaxial strength experiments provides the parameters for determining the failure criteria. While conducting these experiments under dry and saturated conditions provides the ability to assess the impact of saturation on strength, this is not commonly done in commercial applications, where most laboratory experiments (when they are conducted at all) are conducted on dry samples. Considering the small volume of samples available, this study is focussed on the impact of physical characteristics and confinement on strength of dry samples.

We present physical property-rock strength relationships for the southern Taranaki Basin reservoirs, utilizing two independent physical properties, porosity fraction and mean grain diameter, to predict the dependent variable, strength as measured by dry the uniaxial compressive strength (UCS). We use statistical analysis for quantitative assessment of derived empirical relations to provide a level of confidence for further extrapolation. We validate the empirical model using physical properties and dry UCS values from existing petroleum report and published data for two different sandstones. In addition, we present dry triaxial strength data to quantify the effect of confinement on strength and develop failure envelopes for both the Mohr-Coulomb and Generalised Hoek-Brown failure criteria, again exploring the effect of grain size.

2. Geological setting

2.1. Tectonic history

The Taranaki Basin, the only petroleum producing province in New Zealand, is located on the west coast of New Zealand, spanning an area of approximately 330,000 km^2 (Fig. 1). The Taranaki Basin is divided into two main structural components, the Western Stable Platform and the Eastern Mobile Belt (Mcbeath, 1977, Pilaar and Wakefield, 1978; King et al., 1991); separated by the Cape Egmont Fault. The Western Stable platform has remained undeformed since the Late Cretaceous, whilst the Eastern Mobile Belt has experienced significant Neogene Deformation (King and Thrasher, 1996; Nicol et al., 2007). The Late Cretaceous-Early Palaeocene strata reflect the onset, and continuation of, early basin rifting and thermal rift subsidence associated with the West Coast-Taranaki rift phase, with thick depocentres, associated with NE-SW trending fault bound sub-basins, controlled the rate of sedimentation (Thrasher, 1990, 1992; King and Thrasher, 1996). During the Palaeocene-Eocene, passive margin development was associated with the development of a NE-SW trending, wide, marine-influenced, shoreline belt across the central Taranaki Basin (King and Thrasher, 1996). Sedimentation during this time kept pace with passive margin subsidence resulting in intermittent regressive and transgressive movement of the Paleogene shoreline (Higgs et al., 2012). In the Late Eocene, a decrease in subsidence rates resulted in a southwards transgression and marine inundation across the Central and Southern Taranaki Basin. Early rift tectonics were later overprinted by Neogene convergent margin related tectonics (King and Thrasher, 1992).

2.1.1. Maui and Maari-Manaia Fields

The Maui and Maari-Manaia Fields, located within the central southern region of the Taranaki Basin (Fig. 1), contain large accumulations of hydrocarbon reserves, representing significant producers for the Taranaki Basin (King and Thrasher, 1996). The Maui Field is bound by the western Whitiki Fault and the eastern Cape Egmont Fault. A dual crested, low relief, fault-bend-fold anticline, with a spatial extent of 150 km^2, is associated with Neogene compression on the Whitiki Fault, during the Miocene inversion. Subsequent activation of normal movement along the Cape Egmont Fault during the Middle Pliocene extension, acted to enhance structure expression of the fold (King and Thrasher, 1996). The dual crested anticline delineates two regions, the north eastern, gas-bearing Maui A field, and the south western, gas and oil Maui B field. The Maari-Manaia Field, positioned directly south of the Maui Field, is currently New Zealand's largest offshore oil field and covers an area of 80 km^2. The Maari-Manaia Field resource is contained within two anticlines termed the Maari and Manaia fold structures (New Zealand Petroleum & minerals, 2014). The field is bound to the east by the Manaia Fault, with formation of the anticlinal traps associated with inversion of the Maari-Manaia region during Miocene shortening (King and Thrasher, 1996).

2.2. Stratigraphy

The Late Cretaceous to Eocene offshore reservoirs of the Kapuni Group are widely distributed across the Taranaki Basin (Fig. 2). The Kapuni Group subdivides into the upper Mid-Eocene Mangahewa Formation, Early to Mid-Eocene Kaimiro Formation, and Lower Paleocene Farewell Formation. These formations are distributed within a NE-SW trending shoreline belt across the Taranaki Basin, following the paleoshoreline of the Paleogene, superimposed on a passive margin succession (King and Thrasher, 1996; Strogen, 2011; Higgs et al., 2012, 2017). These passive margin formations composed of marginal marine-shallow marine sandstones and coastal plain sandstones, are observed within the Maari-Manaia and Maui Fields, and form most of the petroleum reservoirs in the Taranaki Basin (Higgs et al., 2017). The entire Kapuni Group succession, from the Mangahewa 'C' sands to the Lower Farewell F′ sands, comprises laterally equivalent sedimentation (Higgs et al., 2017). The movement of the shoreline back and forth across the Maui area, and fluctuations in the rate and locus of sediment supply, have resulted in highly cyclic, intercalated coastal plain and shallow marine strata (New Zealand Petroleum & minerals, 2014). The Mangahewa 'C' sands consist of both non-marine and marine sediments, interpreted as deposits of a braid delta or delta plain (Chantellier and Hitchings, 1987). The upper interval of the 'C' sands is comprised of shoreface and tidal sandstones, with inner shelf shales consistent with propagation of braid plain into the marine environment (Chantellier and Hitchings, 1987; Bryant et al., 1994). The lower interval is represented by coastal plain sandstones and lagoonal mudstones consistent with a braided delta plain. The 'D' sands of the Kaimiro Formation consist of mostly nom-marine sediments deposited within an upper delta plain or fluvial estuarine environment (King and Thrasher, 1996). The 'C' sands and 'D' sand deposits have a high degree of lateral continuity (Chantellier and Hitchings, 1987). The 'F' sands of the Farewell Formation are considered significantly more homogenous unit than the overlying 'C' and 'D' sands. The 'F' Sands

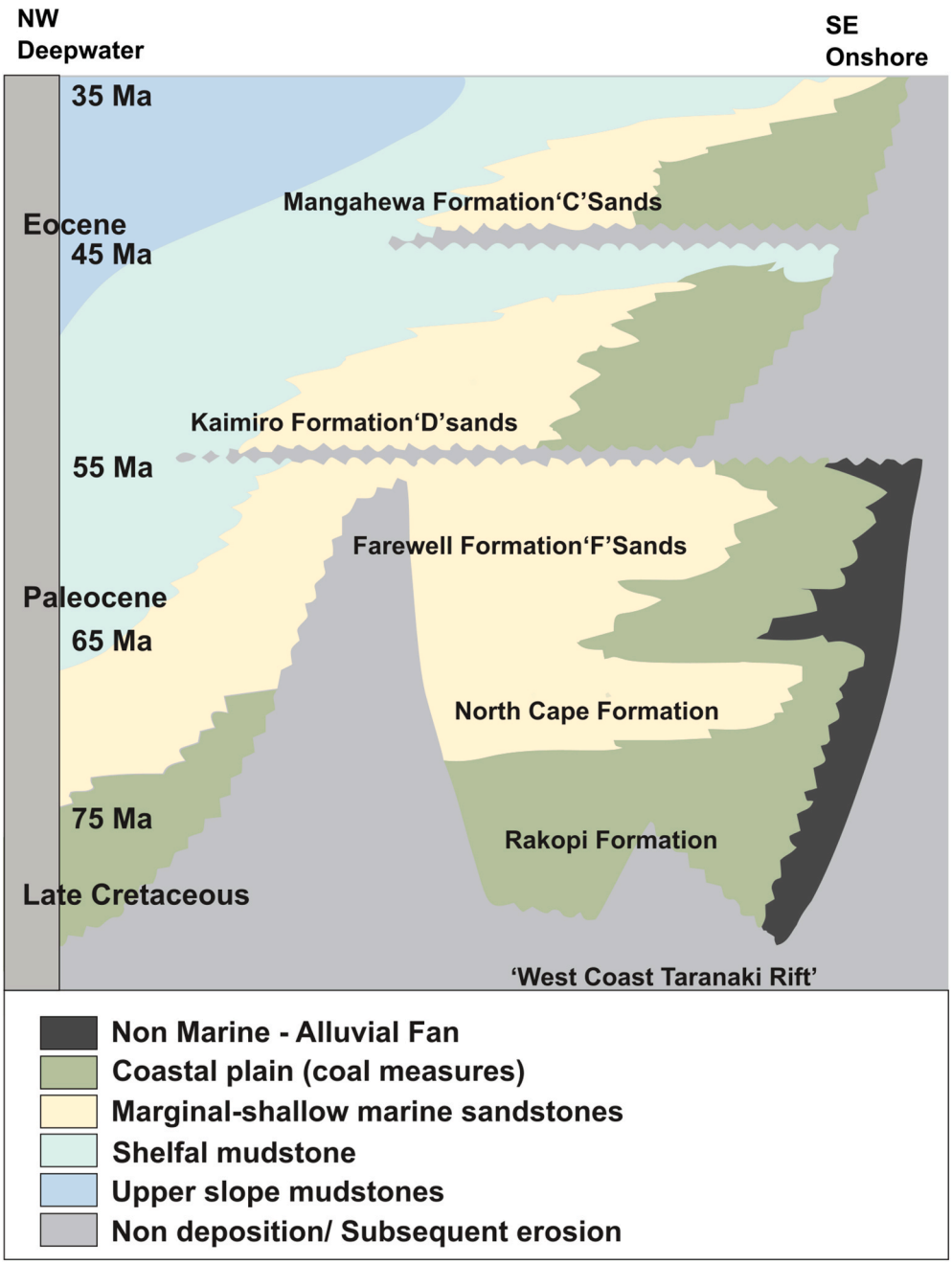

Fig. 2. Generalised stratigraphy of the southern Taranaki Basin, with indication of gross depositional environment. The onset and continuation of the West Coast Taranaki Rift is denoted by the coal rich coastal plain and shallow marine sandstones of the Pakawau group. (Kapuni Group – Mangahewa, Kaimiro and Farewell formations, and Pakawau Group – North Cape and Rakopi formations). Modified from King and Thrasher (1996).

consist of stacked, fining-upwards sequences interbedded with thin coal-shale intervals that are often extensive intra-formation seals (Bryant et al., 1994).

The Late Cretaceous North Cape Formation, a potential reservoir and known source rock in the Taranaki Basin, is the uppermost unit of the Pakawau Group. The North Cape Formation is comprised of shallow marine and coastal sandstones, and localised conglomerates and coal measures (Titheridge, 1977; Bal and Lewis, 1994; Browne, 2009; Strogen et al., 2017; Joyce, 2018). The localised coal-rich facies of the North Cape Formation are a known generating source rock for many producing fields in the Taranaki Basin (Sykes and Dow, 2000; Sykes and Raine, 2008).

3. Methods and materials

3.1. Sampled reservoir intervals

Sample selection was approached in a systematic manner and incorporates four reservoir horizons, Mangahewa 'C' sands, Kaimiro 'D' sands, Farewell 'F' sands and the North Cape formation (Fig. 3). The intervals selected for sampling consist of subfeldsarenite to feldsarenite (categorised according to Folk et al., 1970), with grain percentage ranging from 76 to 85% and authigenic material (clay and quartz cement) ranging from 9 to 23%. Most samples were massive, but when bedding was visible (e.g. Moki 1 'C Sand'), it was perpendicular to the borehole axis. Permission was granted from New Zealand Petroleum and Minerals (NZP&M) to sub-sample core plugs for destructive strength

Fig. 3. Photographs of selected reservoir intervals from petroleum boreholes Moki-1, Maui-A1(G), and MBR (2) used to subsample core plugs for non-destructive and destructive laboratory testing.

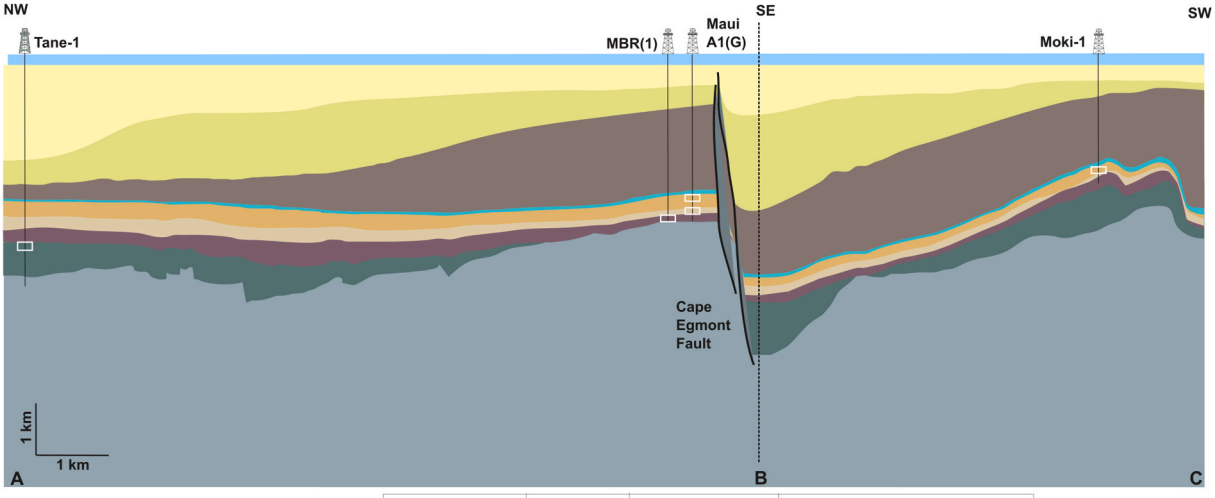

Series/Epoch	NZ Stage	Seismic Horizons	Formation (Reservoir Interval)
Pleistocene	Wn-0	Above N82	
Pliocene	Tk-Wm	N50-N82	
Miocene	Po-Tt	N05-N50	
Oligocene	Lwh-Lw	P50-N05	
Mid-Late Eocene	MdDh-Ar	P22-P50	Mangahewa Formation (C Sands)
Early Eocene	Dw-MdDh	P10-P22	Kaimiro (D Sands)
Paleocene	Dt	P00-P10	Farewell Formation (F Sands)
Upper Cretaceous	Mh	Base-P00	North Cape Formation
Basement		Below Base	

Fig. 4. Cross section A-B-C as positioned in Fig. 1. Transect developed using the GNS PBE 3D Taranaki Map across the study area showing the spatial distribution of wellbores and sampled reservoir intervals. Chronostratigraphy is constrained based upon seismic horizons, with reference to equivalent formation.

testing from five petroleum wells within the Maui and Maari-Manaia fields: Moki-1, Maui-A1(G), MBW(2), MBR (2) and Tane-1 (Table 1). These petroleum wells are predominantly located in the Southern Taranaki Basin within the Maui and Maari-Manaia Fields, with the exception of Tane-1 well which is positioned further northwest in the offshore Taranaki region (Fig. 1). There are minimal well penetrations of the North Cape Formation due to depths in excess of 3500 m (Fig. 4), thus there is limited core availability for this lithology.

3.2. Non-destructive testing

Core plugs were subsampled following standard D4543-19 (ASTM International, 2019) at the NZP&M Featherston Core Store, New Zealand. The 80 cylindrical cores, 25 mm in diameter, were sampled in two orientations were possible: vertical (following the borehole axis) and horizontal (perpendicular to the borehole axis) in order to test rock property variation due to any potential fabric anisotropy effects. Prior to testing, samples are oven-dried for at least 48 h at 60 °C. Sample dimensions and masses are used to determine bulk density measurements (Ulusay and Hudson, 2007). Porosity measurements are acquired from the Micrometrics AccuPycII1340 gas Pycnometer using a high purity nitrogen gas as a displacement medium to accurately measure grain volume at room pressure. The connected porosity is determined as the ratio of pore volume (bulk volume-grain volume) to the bulk volume,

Table 1
Summary of sampled reservoir interval from each wellbore with associated depth range (mMDRT = measured depth below rotary table in metres).

Wellbore		Formation	Depth Range (mMDRT)	Reference
Moki-1		Mangahewa Formation	2134–2139	Tricentrol Exploration Overseas Ltd. (1984)
Maui A1(G)		Mangahewa Formation	2771–2779	Koninklijke/Shell Exploratie (1986)
		Kaimiro Formation	3068–3078	Shell BP Todd Oil Services Ltd (1976)
Maui B	MBR (1)	Farewell Formation	3516–3524	Stos Development Department (1993a)
	MBW (2)	Farewell Formation	4124–4133	Stos Development Department (1993b)
Tane-1		North Cape Formation	3689–3694	Shell BP Todd Oil Services Ltd (1979)

and reported as a fraction from 0 to 1.

Compressional (V_p) and shear wave (V_s) sonic wave velocities are measured, using a GCTS Ultrasonic Velocity Testing System (CATS ULT-100). Two platens are positioned at the top and bottom of the sample. Piezoelectric transducers are used to measure the sonic velocities along the axis of core specimens. A CMT 100 kN load frame is used to apply a small amount of axial load (2 kN) to ensure full contact between sample end surfaces and piezoelectric platens in accordance with Ulusay (2014). Compressional wave velocities, V_p (m/s), are converted to imperial units (ft/s) according to wireline data interpretation and used to determine the compressional slowness, Δt, using Equation (1):

$$DTC = \frac{1}{V_P}\Delta t = \frac{1}{V_P} \tag{1}$$

Sonic velocities (m/s) are used to determine the dynamic Elastic Modulus (GPa) of the samples (Equation (2)), where E is the dynamic Elastic Modulus, and ρ is the sample dry bulk density (kg/m^3).

$$E = \frac{\rho V_s^2\left(3V_p^2 - 4V_s^2\right)}{\left(V_p^2 - V_s^2\right)} \tag{2}$$

3.3. Destructive testing

Of the 80 drill core plugs used for non-destructive testing, 45 were selected for destructive strength testing. All uniaxial and triaxial experiments were conducted on oven-dried samples. The destructive strength testing procedures followed guidelines from standard D7012-14e1 (ASTM International, 2014), including guidelines for uniaxial compressive tests, triaxial compressive strength tests, and elastic moduli calculation from these test result. For all test specimens, a length to width ratio 2:1 is desirable; however, restrictions arose from the inability to drill core plugs of weaker material to a suitable length and 33% of the plugs had a ratio less than 1.55:1. For strength data acquired from samples with a smaller ratio, the results are critically assessed before being utilized in further work, for example using the dimensions to determine whether or not to include outliers.

Uniaxial Compressive Strength (UCS) tests are carried out using a 100 kN load frame (S178 Multi-Tester) commissioned by CMT Equipment, Australia. Experiments are run under a fixed axial strain rate of 1×10^{-5} s^{-1} until rock failure. Real time data of axial load and deformation are measured by a 100 kN load cell and 25 mm axial displacement transducer, respectively, and recorded using LabVIEW software. Due to limited material, all test specimens are considered non-conformable with the suggested minimum sample diameter of 50 mm for UCS testing (tested samples have diameters less than the 50 mm in the ASTM International, 2014 standard). Thus, a correction is applied to all UCS laboratory data as proposed by Hoek and Brown (1980), using Equation (3):

$$\sigma_{cd} = \sigma_{c50}\left(\frac{50}{d}\right)^{0.18} \tag{3}$$

where.

σ_{cd} = measured UCS value (MPa)
d = sample diameter (mm)
σ_{c50} = corrected UCS value for an equivalent 50 mm diameter

Triaxial strength tests are conducted under conventional conditions whereby $\sigma_1 > \sigma_2 = \sigma_3$ (where σ_1, σ_2, and σ_3 are the maximum, intermediate, and minimum principal stresses, respectively). For triaxial tests, each specimen is placed in a rubber sleeve within a Hoek cell, with top and bottom platens in contact with the specimen end surfaces. A small amount of axial load is applied with the 100 kN S178 multitester to hold the platens in place, followed by a manually applied confining pressure via a hydraulic pump to secure the pressure vessel in place. For triaxial tests each specimen is hydrostatically loaded to a selected confining pressure between 5 and 30 MPa ($\sigma_2 = \sigma_3$), then the axial load (σ_1) is increased at a fixed strain rate of 1×10^{-5} s^{-1} until sample failure.

Due to sparse core availability from the wellbores, there is an uneven distribution of test specimens for each formation. The Mangahewa, Farewell and North Cape formations each have >20 data points (UCS and triaxial data), capturing the natural variability in rock properties of these units. The Kaimiro Formation, conversely has only 3 UCS and 2 triaxial data points. This is sufficient to develop a failure criterion for the dataset, but not sufficient to generalise for the entire formation. For this reason, strength characterisation is based upon grain size rather than formation. Grain size analysis was undertaken by a petrographic study on 44 thin sections and corroborated by existing data from other petroleum studies (Higgs et al., 2012). For each thin section a consistent method for grain size determination is taken whereby the diameter of 100–120 grains was measured along their long axes; sample data is given as a mean grain diameter (D).

3.4. Empirical strength relationships

Different physical parameters (porosity, mean grain diameter, compressional slowness and Young's modulus) are plotted against UCS to determine empirical strength relationships. Statistical analyses are performed on the empirical strength relationships to determine the ability for each physical parameter to act as a predictor for strength. A 'P' value was calculated for simple linear bivariate regressions using the least square method, where 'P' is a probability factor that quantitatively assesses the statistical significance of a linear correlation between two variables (Milton and Arnold, 1994). A null hypothesis states there is no relationship between the independent variable (x) and the dependent variable (y). The alternative hypothesis states that if there is a significant linear relationship between the independent variable and the dependent variable, the linear regression slope is not equal to zero. A small 'P' value (we use <0.05) suggests a statistically significant correlation and that the null hypothesis should be rejected, in support of the alternative hypothesis (Rawlings et al., 2001).

3.5. Development of failure criteria

An empirical failure criterion can be used to establish the strength of a rock in terms of the minor and major principal stresses σ_1 and σ_3. The Generalised Hoek-Brown criterion (Equation 4) uses a non-linear relationship and is defined by the major and minor principal stresses based upon the unconfined compressive strength of intact rock (σ_{ci}, in MPa) and a material constant (mi) (Eberhardt, 2012). The material parameter 'mi' is analogous to the frictional strength of the rock. Note that σ_{ci} (unconfined compressive strength) is the intersection of the Hoek-Brown failure envelope with the σ_1 axis and is not the same as the laboratory

UCS (uniaxial compressive strength), although the values should be similar. Both empirical fit parameters, σ_{ci} and mi, are unique to each lithology, and are derived using the uniaxial and triaxial test data.

$$\sigma_1 = \sigma_3 + \sigma_{ci}\left(m_i\frac{\sigma_3}{\sigma_{ci}} + 1\right)^{0.5} \quad (4)$$

Many geo-engineering programs utilize the Mohr-Coulomb failure criterion for input parameters. The Mohr Coulomb failure criterion (Equation (5)) imposes a linear relationship and is defined by an angle of internal friction (φ, in degrees) and cohesion (C, in MPa).

$$\sigma_1 = \frac{2C\cos\varphi}{1-\sin\varphi} + \frac{1+\sin\varphi}{1-\sin\varphi}\sigma_3 \quad (5)$$

The spreadsheet developed by Villeneuve and Heap (2021) is used to employ a regression of the triaxial data to derive both Hoek-Brown and Mohr-Coulomb parameters. For the Hoek-Brown parameters, Equations (6) and (7) are used (Hoek and Brown, 1997):

$$\sigma_{ci} = \sqrt{\frac{\sum y}{n} - \left[\frac{\sum xy - \left(\frac{\sum x \sum y}{n}\right)}{\sum x^2 - \left(\frac{(\sum x)^2}{n}\right)}\right]}\frac{\sum x}{n} \quad (6)$$

$$m_i = \frac{1}{\sigma_{ci}} - \left[\frac{\sum xy - \left(\frac{\sum x \sum y}{n}\right)}{\sum x^2 - \left(\frac{(\sum x)^2}{n}\right)}\right] \quad (7)$$

where $x = \sigma_3$, $y = (\sigma_1 - \sigma_3)^2$, and n is the number of triaxial tests. Note that Equation (6) is based on the worked example, not Equation B2, from Hoek and Brown (1997).

To determine the Mohr-Coulomb parameters the triaxial data are plotted in radius space (Craig, 1997; Villeneuve and Heap, 2021), where the x axis is mean normal stress $(\sigma_m) = (\sigma_1 + \sigma_3)/2$, and the y axis is the maximum shear stress $(\tau_m) = (\sigma_1 - \sigma_3)/2$. A linear fit through the data points in radius space provides two fitting parameters, 'a' and 'f' such that: $\tau_m = \sigma_m a + f$. The Mohr-Coulomb failure criterion expressed in radius space as $\tau_m = \sigma_m \sin\varphi + C\cos\varphi$ and the parameters 'a' and 'f' are used to solve for internal friction angle, φ, and cohesion, C, using Equations (8) and (9):

$$\varphi = \sin^{-1} a \quad (8)$$

$$C = \frac{f}{\cos\varphi} \quad (9)$$

The standard error of the 'a' and 'f' coefficients are calculated using the spreadsheet from Villeneuve and Heap (2021) and propagated through to the φ and C.

Table 2
Summary of physical rock properties and uniaxial compressive strength tests for each test specimen (core plug samples three directions, vertical (v) and two orthogonal horizontal directions (h1 and h2).

Sample Code	Depth (m)	Core plug direction	Mean Grain Diameter D (μm)	Porosity Fraction n	Vp Dry (m/s)	Compressional Slowness DTC (μs/ft)	Young's Modulus (GPa)	UCS (MPa)	
								Measured σ_{cd}	Corrected σ_{c50}
MK1-B10	2134.3	v	215	0.11	2506	121.63	12.5	31.06	27.38
MK1-B10	2134.6	h2	215	0.09	2296	132.75	11.2	28.94	25.52
MK1-B11	2135.6	h1	213	0.16	2165	140.79	8.5	20.15	17.77
MK1-B12	2136.4	v	169	0.14	2258	134.99	10.4	24.58	21.68
MK1-B12	2136.4	h1	169	0.12	2528	120.57	12.7	24.61	21.69
MK1-B13	2137.4	v	189	0.13	2231	136.62	8.8	27.12	23.91
MK1-B14	2138.5	h2	136	0.08	2543	119.86	14.8	31.67	27.90
A1G-B6B	2771.3	v	101	0.18	2824	107.93	12.6	23.23	20.48
A1G-B6B	2771.3	h1	101	0.21	2614	116.6	8.8	41.12	36.20
A1G-B7	2774.0	v	109	0.20	2498	122.02	12.7	28.57	25.17
A1G-B10A	2776.7	v	172	0.16	2420	125.95	10.1	15.28	13.47
A1G-B10A	2776.7	h1	172	0.17	2737	111.36	10.8	25.51	22.48
A1G-B10B	2777.9	h2	209	0.15	2845	107.14	9.6	27.17	23.95
A1G-B10B	2777.9	v	209	0.16	2734	111.49	9.5	39.51	34.83
A1G-B1	3068.5	h1	197	0.14	2912	104.67	13.4	30.55	26.94
A1G-B1	3068.5	v	197	0.12	2457	124.05	13.5	65.50	57.76
A1G-B2	3069.7	v	171	0.09	2653	114.89	9.0	38.35	33.82
MBR-B2	3516.9	h1	233	0.15	2381	128.01	8.4	27.37	24.13
MBR-B7	3521.8	v	272	0.21	2249	135.53	10.5	14.95	13.17
MBR-B7	3521.8	h1	272	0.20	2498	122.02	8.9	16.38	14.44
MBR-B8	3522.8	v	108	0.15	2183	139.62	9.8	46.43	40.91
MBR-B9	3523.4	v	102	0.15	2420	125.95	8.2	53.40	47.05
MBR-B9	3523.4	h1	102	0.16	2460	123.9	7.9	62.56	55.11
MBW-B8	4124.7	h2	183	0.19	2541	119.95	16.0	17.34	15.27
MBW-B8	4124.7	v	183	0.19	2099	145.21	13.9	22.69	20.01
MBW-B12	4128.1	h1	215	0.19	2606	116.96	26.2	26.60	23.45
MBW-B12	4128.1	v	215	0.20	2773	109.92	28.8	28.56	25.18
MBW-B14	4130.4	h1	265	0.22	2226	136.93	11.0	14.95	13.17
MBW-B16	4132.5	v	222	0.23	2195	138.86	13.1	18.01	15.88
T1-B2	3689.2	h2	55	0.08	3409	89.41	16.1	57.08	50.23
T1-B3	3689.9	h1	63	0.07	3683	82.759	12.9	66.29	58.43
T1-B3	3689.9	v	63	0.06	2160	141.11	16.7	67.20	58.89
T1-B4A	3692.4	v	126	0.12	1950	156.31	12.4	40.82	35.98
T1-B4B	3692.0	h1	152	0.11	2606	116.96	8.9	17.53	15.44
T1-B4B	3692.0	v	152	0.11	1944	156.79	14.4	45.63	40.23
T1-B5	3693.7	h1	173	0.15	2390	127.53	12.4	26.36	23.20
T1-B5	3693.7	v	173	0.14	2075	146.89	11.8	28.80	25.39

4. Experimental results

4.1. Physical and uniaxial compressive strength measurements

For all samples tested, UCS values range from 9 to 67 MPa, porosity fractions fall between 0.05 and 0.24, compressional slowness varies from 75 to 150 μs/ft, and Young's moduli fall between 7.9 and 28.8 GPa (Table 2). Mean grain diameter (D) varies from 55 to 363 μm (Table 2), representative of coarse-grained silts to medium grained sands (Folk, 1963). Where experiments were conducted on core axis parallel and core axis perpendicular samples for the same interval, the ratio of vertical to horizontal strength was found to range from 0.56 to 2.6, with one outlying ratio of 5, showing no systematic anisotropy. The UCS shows a general negative correlation with increasing porosity fraction (Fig. 5a), increasing compressional slowness (Fig. 5b), and increasing mean grain diameter (Fig. 5c), and a general positive correlation with increasing Young's modulus (Fig. 5d).

The linear relationship for porosity fraction-UCS has a 'P' value of 3.92 x10-5, for compressional slowness-UCS a 'P' value of 0.196, for mean grain diameter-UCS a 'P' value of 4.42 x10-6, and for Young's Modulus-UCS a 'P' value of 0.370. The small 'P' values attributed to the porosity fraction-UCS and mean grain diameter-UCS series suggests statistically significant correlations. The higher 'P' values attributed to the compressional slowness-UCS and Young's Modulus-UCS are above the 0.05 threshold, making these test inconclusive and the relationships statistically unsound. For this reason, the porosity fraction-UCS data and mean grain diameter-UCS series provide the strongest empirical relations for our data set.

4.2. Triaxial experiments

Triaxial experiment results are summarised in Table 3. Increasing confining pressure results in an increase of axial stress required to cause rock failure, as observed in previous studies of triaxial deformation of sandstone (Wong et al., 1997; Baud et al., 2000; Bésuelle et al., 2003; Heap et al., 2019).

Fig. 6 compares differential stress versus axial strain curves for three different sandstones from MBR (1), MBW(2), and Tane 1 at a confining pressure of 10 MPa (~0.5UCS). The stress-strain curves exhibit similar initial linear elastic trends but different yield responses. MBW-B8h1 and T1-B3h2 display abrupt failure, yielding behaviour that is indicative of dilatant microcracking dominant deformation (Heap et al., 2015; Siratovich et al., 2016). MBR-B9h2 exhibits a gradual yield curve that is indicative of mixed dilatant microcracking and compaction deformation (Heap et al., 2015; Siratovich et al., 2016). The brittle deformation resulting from failure in samples MBW-B8h1, MBR-B9h2 and T1-B3h2 is defined by a plane of failure along a shear fracture inclined approximately 60° to the sample core axis. This suggests there is no systematic effect of either grain diameter or porosity on the brittle deformational behaviour of these rocks under low confinement.

4.3. Failure criteria

Triaxial data are plotted in Fig. 7 in two different stress spaces to derive the Hoek-Brown failure criterion parameters (principal stress space, Fig. 7a) and the Mohr Coulomb failure criterion parameters (radius stress space, Fig. 7b; Craig, 1997; Villeneuve and Heap, 2021). The resulting parameters are given in Table 4. These results are in agreement with Robertson (1970), that whilst recognising considerable variation on the scatter plot, the cohesion is between 16 and 27% of the average UCS value.

For the well MBR interval tested (porosity fraction 0.13–0.21) the two grain size fractions, silts-very fine sand (102–108 μm) and fine-medium sand (233–272 μm) demonstrate, that the finer grained samples have higher strength than the coarser grained samples (Fig. 7). The effect of grain size on rock strength is further demonstrated, with comparison of grain diameter and the two failure parameters derived for the Hoek-Brown (σ_{ci} and m_i) Mohr-Coulomb criterion (cohesion and φ) (Fig. 8). For samples with a similar porosity fraction ranging between 0.12 and 0.21, the m_i and φ (which describe the curvature and slope of the failure criteria, respectively) increase with increasing grain diameter (Fig. 8a), whilst the σ_{ci} and cohesion (which describe the low-confinement strength components of the failure criteria) decrease with increasing grain diameter (Fig. 8b). This shows that while the strength decreases with increasing grain diameter, the effect increasing confinement on strength is more pronounced for coarser samples than for finer samples. No relationships could be observed between porosity fraction and the Hoek-Brown criterion parameters σ_{ci} and m_i, nor the

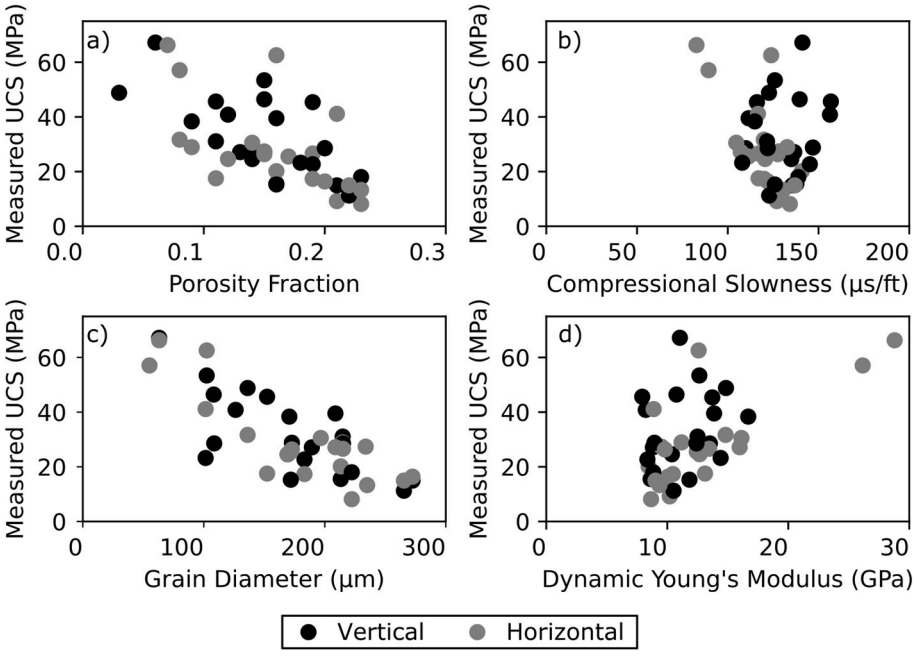

Fig. 5. Physical property-UCS data series, a) porosity fraction-UCS; b) compressional slowness-UCS; c) mean grain diameter-UCS; d) dynamic Elastic modulus-UCS.

Table 3
Summary of triaxial data (core plug samples three directions, vertical (v) and two orthogonal horizontal directions (h1 and h2).

Sample Code	Series Name	Depth (m)	Core plug direction	Maximum Principal (Axial) Stress (σ_1)	Minimum Principal (confining) stress ($\sigma_2 = \sigma_3$)	Mean Grain Diameter D (μm)	Porosity Fraction n
MK1-B11	Moki 1	2135.6	h2	101	15	213	0.15
MK1-B12		2136.4	h2	75	5	169	0.13
MBR-B2	MBR-1	3516.9	h2	128	15	233	0.17
MBR-B7	(coarse)	3521.8	h2	67	5	272	0.19
MBR-B8	MBR-1 (fine)	3522.8	h1	139	20	108	0.15
MBR-B9		3523.4	h2	134	10	102	0.13
MBW-B8	MBW-2	4124.7	h1	93	10	183	0.20
MBW-B14		4130.4	h2	57	5	265	0.22
MBW-B16		4132.5	h2	68	7	222	0.24
T1-B4A	Tane 1	3692.4	h1	114	15	126	0.12
T1-B4B	(coarse)	3692.0	h2	134	20	152	0.10
T1-B3	Tane 1 (fine)	3689.9	h2	115	10	63	0.09
T1-B2		3689.2	h1	147	25	55	0.08

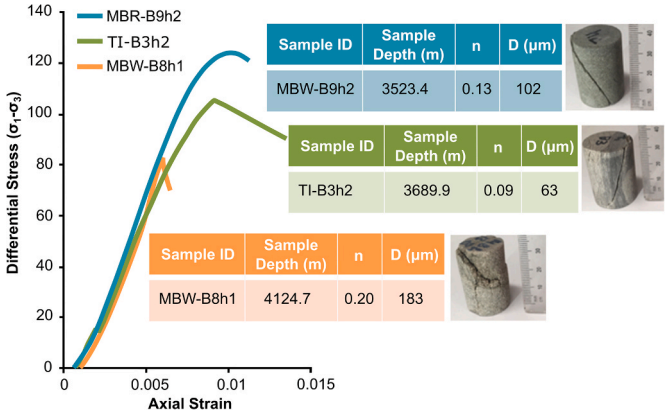

Fig. 6. Differential stress versus axial strain curves for three different samples under a confining stress of 10 MPa, exhibiting different modes of yield.

Mohr-Coulomb parameters, C and φ, in contrast to what has been found for volcanic rocks (Villeneuve and Heap, 2021).

5. Discussion

5.1. Empirical strength relationships derived from sandstone reservoir

The use of empirical relationships utilizing more than one independent variable for sandstone rock strength prediction is infrequent (Moos et al., 2001; Chang et al., 2006; Fjaer et al., 2008); particularly those that incorporate petrophysical property parameters such as grain size, clay volume or cement content (Ulusay et al., 1994; Atapour and Mortazavi, 2018). Numerical simulations provide interesting indications of how physical characteristics affect mechanical parameters by controlling individual characteristics directly, which is clearly difficult for natural rock specimens. For example Xu et al. (2020), via numerical simulations, showed that grain size distribution also impacts strength, suggesting that grain size distribution is worth collecting in addition to mean grain size. We focussed our investigations on porosity and mean grain diameter because they are easy to measure and have been shown to correlate well to strength (porosity: Bell, 1978, Vernik et al., 1993, Ulusay et al., 1994; Baud et al., 2014; grain size: Fredrich et al., 1990; Hoek et al., 1992; Wong et al., 1997; Carbillet et al., 2021). Our results, focussed on porosity and mean grain diameter, indicate that both provide strong controls on sandstone UCS (Fig. 5), however other parameters, such as grain size distribution, cementation and mineralogical content are also candidates for focussed study.

Most studies agree that porosity and UCS exhibit an inverse relationship (Bell, 1978; Vernik et al., 1993; Ulusay et al., 1994). This is also what is predicted by the pore-crack model of Sammis and Ashby (1986),

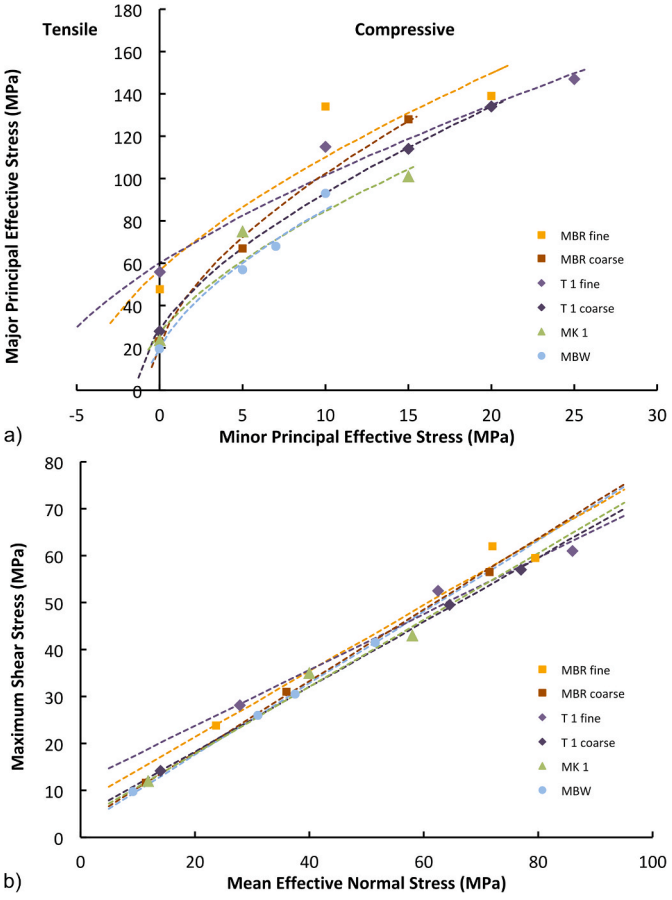

Fig. 7. All triaxial test data plotted in a) principal stress space to derive the Hoek-Brown failure criteria; b) radius stress space to derive the Mohr-Coulomb failure criteria according to Craig (1997) and Villeneuve and Heap (2021). (For interpretation of the references to colour in this figure legend, the reader is referred to the Web version of this article.)

as discussed in Baud et al. (2014). Previously proposed porosity-UCS relationships have been characterised by linear, logarithmic, power, exponential, and second order polynomial laws (Vernik et al., 1993; Palchik, 1999; Chang et al., 2006; Reyer and Philipp, 2014). Localised calibration through laboratory testing manipulates the correlation coefficients in the regressions to increase the accuracy and better fit the data. Data from this study suggest that the porosity-UCS relationship could be defined by multiple regression types, all displaying similar regression coefficients (r^2) (Palchik, 1999; Atapour and Mortazavi, 2018). Most established relationships use an exponential fit, and here we

Table 4
Hoek-Brown (σ_{ci} - empirically derived UCS, m_i - Hoek-Brown constant) and Mohr-Coulomb (C - cohesion; φ - friction angle) Failure criterion parameters derived from triaxial test results for reservoir intervals.

Well	Depth Interval	Mean Grain Diameter (μm)	Porosity Fraction	UCS range (MPa)	Hoek Brown Failure Parameters			Mohr Coulomb Failure Parameters	
					σ_{ci} (MPa)	m_i	Normalized m_i (m_{in})	C (MPa)	φ
Tane-1 (coarse)	3692.0–3693.7	126–173	0.11–0.15	15.4–40.2	29	21	0.7	6 ± 1	44 ± 1
Tane-1 (fine)	3689.2–3689.9	55–63	0.06–0.09	50.2–58.9	60	8	0.1	15 ± 3	36 ± 3
Moki-1	2134.6–2138.5	136–215	0.08–0.16	17.7–27.9	27	18	0.7	5 ± 2	44 ± 4
MBW-2	4124.7–4132.5	183–265	0.19–0.24	13.2–25.2	17	34	2.0	3 ± 1	49 ± 1
MBR-1 (coarse)	3516.9–3521.8	233–272	0.15–0.21	13.2–24.1	23	35	1.5	5 ± 1	49 ± 2
MBR-1 (fine)	3522.8–3523.4	102–108	0.13–0.16	40.9–55.1	57	12	0.2	12 ± 4	42 ± 5

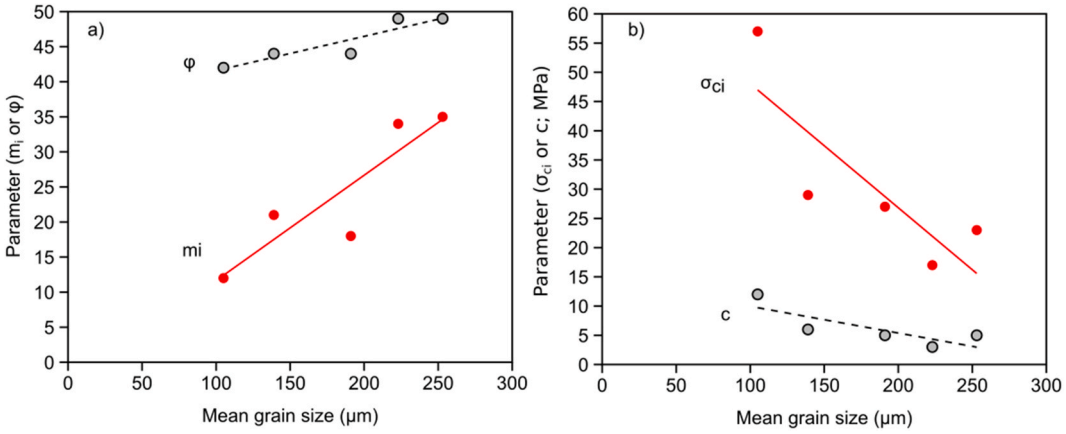

Fig. 8. Mean grain diameter versus Hoek-Brown and Mohr-Coulomb failure criterion parameters for samples with porosity fraction 0.12–0.21 plotted according to a) curve parameters (φ and m_i); and b) strength parameters (C and σ_{ci}). (For interpretation of the references to colour in this figure legend, the reader is referred to the Web version of this article.)

adopt a similar fit, calibrated to our laboratory data (Fig. 9a; Equation (10)).

$$UCS = 108e^{-10n} \quad (10)$$

This empirical relationship uses the formulation for the exponent given in Chang et al. (2006) and follows the general form for the porosity-UCS relationship used in other studies on sandstone empirical relationships (e.g. Reyer and Philipp, 2014; Atapour and Mortazavi, 2018). A linear version of the fit is used in order to simplify for multivariate linear regression and test for goodness of fit, as follows: UCS = 108i, where $i = e^{(-10n)}$, e is the natural logarithm and n is the porosity fraction as a decimal, not a percentage. Using a linear regression of the linear version results in an r^2 value of 0.34 with a 'P' value of 1.557×10^{-4}, showing that the correlation is valid, but with considerable scatter (Fig. 9b).

The role of mean grain size affecting rock strength is a disputed subject, with researchers reporting conflicting results. Previous investigations on low porosity rocks e.g. limestone and marble, have implied rock strength is inversely related to grain size, with a good linear correlation between UCS and the inverse square root of mean grain size (Fredrich et al., 1990; Wong et al., 1996). Studies focused on sandstones have demonstrated a weak correlation between mean grain size and UCS (Shakoor and Bonelli, 1991; Palchik, 1999; Atapour and Mortazavi, 2018).

Our results exhibit an inverse relationship between mean grain diameter, D (μm) and UCS (MPa) (Fig. 9c; Equation (11)), defined as a function of inverse square root mean grain diameter similar to that reported by Fredrich et al. (1990) and Wong et al. (1996). The correlation given in Equation (11) is implicit in the well-known wing crack model of Ashby and Sammis (1990), since most previous studies considered that the size of the microcracks scales with the grain diameter, as described by Baud et al. (2014).

$$UCS = 366\left(\frac{1}{\sqrt{D}}\right) \quad (11)$$

To enable a linear regression and goodness of fit tests, UCS is linearized as UCS = 366j where $j = D^{-0.5}$. In this formulation, the r^2 value for this determined linear relationship is 0.51 and the 'P' value is 6.14×10^{-7}, which, similarly to the porosity-UCS function, is statistically valid, but with some scatter (Fig. 9d). The discrepancies between different studies suggest grain diameter alone is not a suitable indicator of compressive strength in sandstone. Atapour and Mortazavi (2018) show that higher porosity (e.g. above 0.15) reduces the influence of grain size on UCS, and at porosity above 0.3 grain size no longer has an impact on strength.

Formulating an empirical relation for UCS prediction requires a best fit regression attributed to both the porosity fraction-UCS and mean grain diameter-UCS data series. In order to obtain a stronger empirical formula, a multivariate regression was undertaken, which requires the input parameters to be considered independent variables. Theoretically porosity is independent of grain size, and it is the role of alternative petrophysical properties that control the availability of pore space e.g. grain sorting, grain shape/packing and the degree of cementation (Bell, 1978; Shakoor and Bonelli, 1991; Hill, 2020). However, several studies have found this is not the case and that porosity can be seen to increase with mean grain size (Ulusay et al., 1994). The linear relationship of porosity fraction and mean grain diameter is attributed an r^2 value of 0.22 with a 'P' value of 0.003, which is smaller than the 0.05 threshold suggesting a statistically significant correlation between the two variables. This is a much weaker relationship than the relationships with UCS and for the purpose of the analysis the two parameters are considered independent variables.

Fig. 10 exhibits the spatial distribution of data points from the

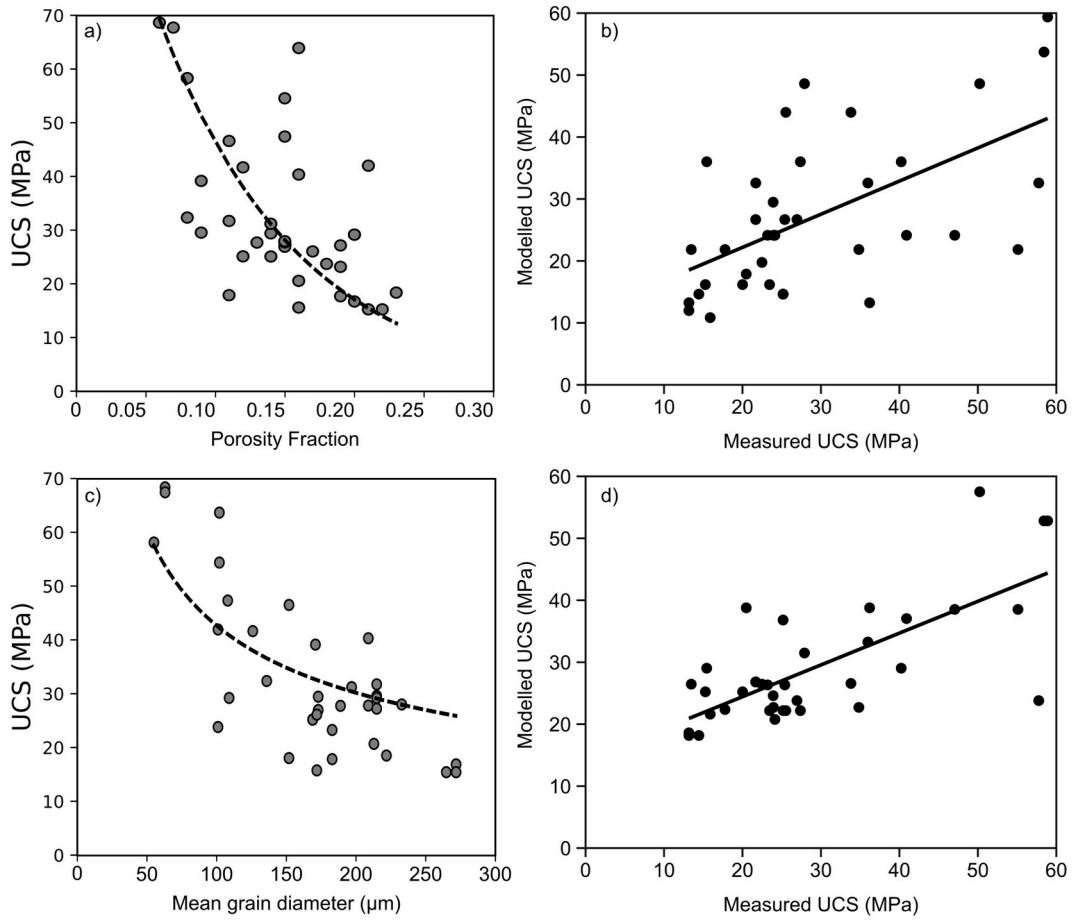

Fig. 9. Plots for a) relationship between porosity fraction and UCS; b) porosity-UCS model prediction performance; c) relationship between mean grain diameter and UCS; d) mean grain diameter-UCS model prediction performance.

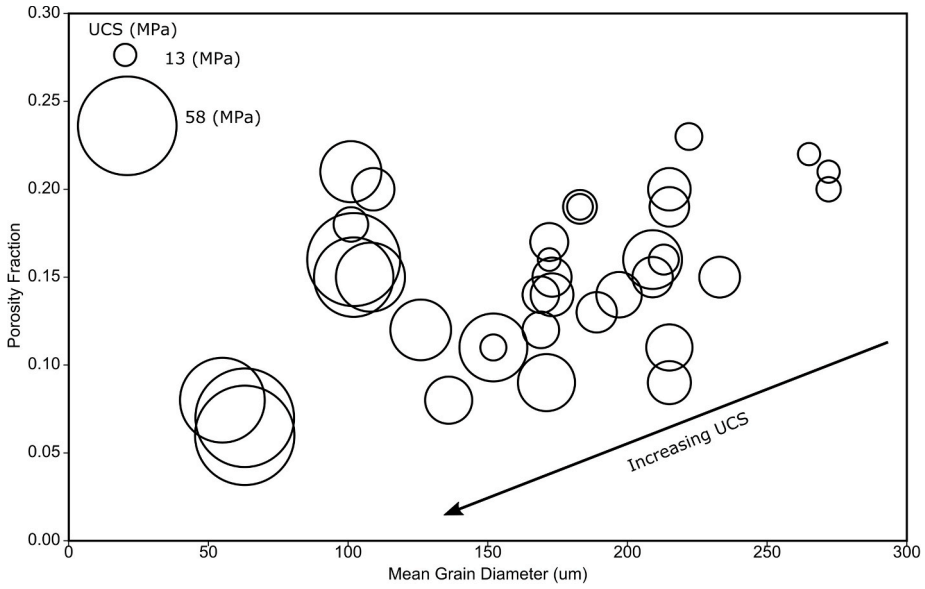

Fig. 10. 3D spatial distribution of the multivariate relationship between independent variables porosity fraction and mean grain diameter, and dependent variable UCS.

porosity fraction-mean grain diameter-UCS data series as a bubble plot where the circle size is representative of UCS magnitude. This shows that UCS increases as both grain diameter and porosity fraction decrease. In practical terms, direct measurements of both porosity and grain diameter are straightforward and achievable and can easily be used in tandem to solve an empirical function for UCS. For the purpose of a multivariate linear regression, UCS is expressed as a function of porosity fraction and inverse square root mean grain diameter, with fitting

parameters calibrated to the dataset presented herein. Regression coefficients calibrated to the dataset were determined by multiple linear regression analysis using the *sklearn* machine learning module of Python (Equation (12)).

$$UCS = \omega_1 \left(\frac{1}{\sqrt{D}}\right) + \omega_2 e^{-10n} - \omega_3 \quad (12)$$

where UCS is the Uniaxial Compressive Strength (MPa), D is the mean grain diameter (μm), n is the porosity fraction, and $\omega_{1\text{-}3}$ are the regression coefficients (given in Table 5).

To provide an overall measure of how well the empirical relationship proposed in Equation (12) fits the data, laboratory measured UCS and corresponding predicted UCS are compared in Fig. 11a. The linear relationship between laboratory measured and modelled UCS values from our data is defined by a an r^2 value of 0.58 with a 'P' value of 3.34×10^{-8} providing confidence in the empirical equation.

In order to assess the validity of the model, existing UCS data are sourced from petroleum reports of the Eocene sands from the Pohokura Field (Shell Todd Oil Services Ltd, 2002) in the north eastern Taranaki Basin (Fig. 1). The test data are summarised in Table 6, including mean grain diameter, porosity fraction, and dry laboratory measured UCS. The linear relationship between modelled UCS using Equation (12) and measured UCS exhibits a r^2 value of 0.48 with a 'P' value of 1.54×10^{-3} (Fig. 11a) but underestimates UCS. This underestimation of UCS could be due to low porosities attributed to the Pohokura samples (0.08–0.12), such that grain diameter has a much stronger impact ('P' value of 7.1×10^{-4}) on strength compared to porosity ('P' value of 0.87). This is in agreement with Atapour and Mortazavi (2018), who show lower porosity (<0.15) increases the influence of grain size on UCS.

Using Equation (12) with the fitting parameters calibrated to the Pohokura data (Table 5) results in a better correlation between measured and predicted UCS (Fig. 11a). Despite the disparate location of both the Pohokura and Maui-Maari reservoir samples, this work suggests the calibration of correlation coefficients from empirical strength relationships to different Taranaki reservoirs, can provide a first estimate of dry UCS for other reservoir intervals. We also tested the model on the dry and saturated sandstone UCS strengths from Heap et al. (2019). Again, calibration was required, but the modelled UCS values provide good strength estimates (Fig. 11b; Table 5). This suggests that the model in Equation (12) is not only applicable to dry strength of rocks from the Taranaki reservoirs, but can also be used to estimate strength for other sandstones, whether dry or saturated.

5.2. Failure criteria

Failure criteria can be used to predict the state stress that results in rock failure, presented as a function of normal (σ_n) and shear stress (τ), or the minimum (σ_1) and maximum (σ_3) principal stresses. The Mohr-Coulomb and Hoek Brown failure criteria are plane stress failure criteria and ignore the effect of the intermediate principal stress (σ_2) (Zoback, 2010). The Mohr-Coulomb criterion is commonly favoured in reservoir geomechanical application due its simplicity as an effective linear prediction tool, expressed in terms of a constant value of cohesion (C) and friction angle (φ). The Hoek-Brown failure criterion is commonly used for rock geotechnics, particularly for slope stability analysis and tunnelling, and its application in reservoir geomechanics is not extensive. Each failure criterion has advantages and disadvantages in their applications. A practical disadvantage of the Hoek-Brown criterion is the absence of published literature relating the material constant (m_i) to commonly measured physical properties from geophysical logs (Zoback, 2010); an advantageous factor is the ability to incorporate rock mass properties (material constants that vary by lithotype) into the failure criterion (Eberhardt, 2012) for mass characterisation of reservoirs (Villeneuve et al., 2018; Heap et al., 2019). Failure criteria assume isotropic conditions in order to function, which is largely not representative of most hydrocarbon resource lithologies. In general, sandstones are classified as isotropic or low anisotropy rocks, regardless of internal structure (Ramamurthy, 1993), however Baud et al. (2005) and Griffiths et al. (2017) show that the uniaxial compressive strength of rocks, including sandstones, can indeed be anisotropic. We conducted our triaxial experiments on samples orientated both parallel and perpendicular to the wellbore axis (horizontal) to explore this, and the UCS results used to generate our empirical relationships show no strength anisotropy at the laboratory scale for this dataset. This could be because any isotropy that is present is at a larger scale than the samples, or that other physical differences, such as grain size or porosity, hide any effects of anisotropy.

The values for m_i range from 8 to 35 (Table 3), which is much wider than the 17 ±4 proposed by Hoek and Marinos (2000) but similar to the range given in Douglas (2002) and Sabatakakis et al. (2018). Given the wide range of m_i values, rather than proposing a range for the sandstones in the Taranaki Basin, the approach developed by Shen and Karakus (2014) to define m_i based on UCS is explored for this dataset. The m_{in} (normalized $m_i = m_i/\sigma_{ci}$) is plotted against σ_{ci} (Fig. 12a) and a power function is fit to the data to derive two parameters, a and b (Equation (13)):

$$m_{in} = a\sigma_{ci}^{b} \quad (13)$$

The m_{in} is also plotted against average UCS and its power function parameters are compared to those obtained from the power function fit to the σ_{ci} data. The 'a' and 'b' fitting parameters for both σ_{ci} and UCS functions are 791 and -2.08, and 2018 and -2.39, respectively. Fig. 12b shows that the predicted m_{in} based on σ_{ci} and UCS both provide suitable estimates of measured m_{in}. These parameters are quite different from those derived for sandstones examined by Shen and Karakus (2014), and Vásárhelyi et al. (2016), however the strengths of the sandstones in this study are at the lower end of the range examined in those studies. Vásárhelyi et al. (2016) also showed that the fitting parameters for a single lithology type (e.g. limestone, sandstone, granite, coal) can vary significantly from one locality to another. By assuming that UCS is $\sim\sigma_{ci}$, m_i could then be estimated using Equation (13) and the Hoek-Brown failure criterion could be derived for reservoir sandstones in offshore Taranaki without necessitating triaxial strength data. In cases where UCS is not available from laboratory testing, it can be estimated using Equation (12). The impact of saturation on these parameters would be worth exploring for sandstone in general as well as for the Taranaki reservoir rocks in particular.

Table 5
Summary of multiple linear regression results for Equation (12) calibrated to the datasets from the Taranaki basin and the Buntsandstein from the Rhine Graben (France; Heap et al., 2019)). Regression coefficients $\omega_{1\text{-}3}$ are for the calibration of Equation (12), whereas the goodness of fit, r^2 and 'P' value, are for the comparison between modelled and measured UCS.

Dataset	Regression coefficients			Model goodness of fit	
	ω_1	ω_2	ω_3	r^2	'P' value
This Study	334	46	−6	0.64	3.42 × 10-9
Pohokura	670	14	3	0.6	1.6 × 10-4
Buntsandstein Dry	1344	274	−66	0.78	2.07 × 10-9
Bundsandstein Saturated	916	202	−51	0.69	1.29 × 10-7

5.3. Application to offshore reservoirs in the Maui Field

Predicting the distribution of mechanical properties across a reservoir interval requires a fundamental understanding of the controls on the rock properties used for strength prediction. Stochastic modelling, determining flow capabilities of a reservoir, utilizes the distribution of sedimentary facies to extrapolate quantifiable physical property data across an interval. Chantellier and Hitchings (1987) determine average physical reservoir properties attributed to different sandstone facies

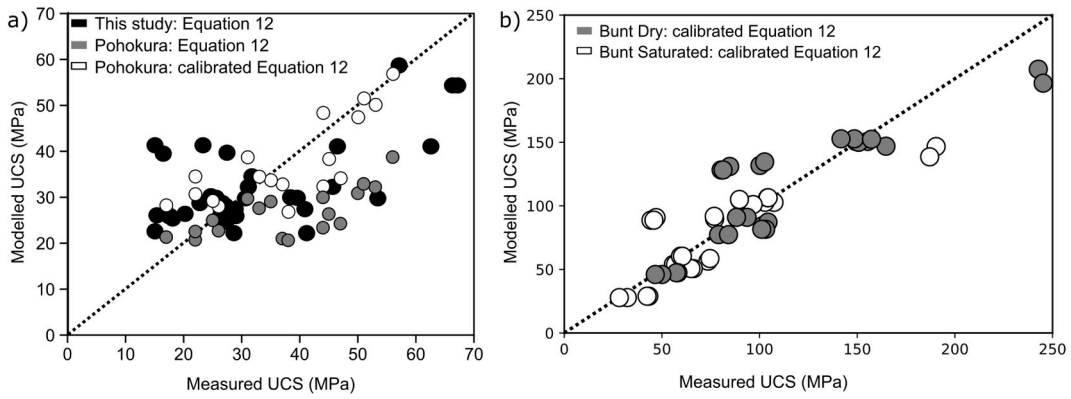

Fig. 11. Comparison of measured to modelled UCS for a) the training data in this study using Equation (12) and the test data from Pohokura using Equation (12) and calibrated Equation (12); b) the dry and saturated test data for the Buntsandstein from Heap et al. (2019) using a calibrated Equation (12). Dashed line represents the 1:1 line.

Table 6
Physical and geomechanical properties used for strength prediction of Pohokura-1 and Pohokura-2 (data are sourced from Martin, 2001; Shell Todd Oil Services Limited, 2001; and Shell Todd Oil Services Ltd, 2002). Laboratory UCS is the value derived from UCS testing.

Wellbore	Depth (m)	Formation	Sample Code	Core Plug Direction	Mean Grain Diameter (μm)	Porosity Fraction n	Laboratory UCS (MPa)
Pohokura-1	3528.3	Maui	U01	h	660	0.10	47
Pohokura-1	3546.8	Maui	U02	h	198	0.08	56
Pohokura-2	3576.8	Maui	U04	h	680	0.12	37
Pohokura-2	3577.4	Maui	U05	h	760	0.10	44
Pohokura-2	3578.5	Maui	U06	h	580	0.13	22
Pohokura-2	3579.7	Maui	U07	h	877	0.10	22
Pohokura-2	3581.2	Maui	U08	h	790	0.07	35
Pohokura-2	3582.6	Maui	U09	h	516	0.08	31
Pohokura-2	3591.5	Maui	U10	h	1190	0.09	26
Pohokura-2	3591.9	Maui	U11	h	1270	0.10	38
Pohokura-2	3593.1	Maui	U12	h	1120	0.08	25
Pohokura-2	3595.4	Maui	U13	h	1100	0.10	17
Pohokura-2	3613.5	Maui	U15	h	490	0.10	45
Pohokura-2	3617.6	Maui	U16	h	702	0.08	33
Pohokura-2	3617.9	Maui	U17	h	290	0.10	50
Pohokura-2	3623.3	Maui	U18	h	254	0.10	53
Pohokura-2	3624.2	Maui	U19	h	238	0.10	51
Pohokura-2	3629.1	Maui	U20	h	270	0.11	44

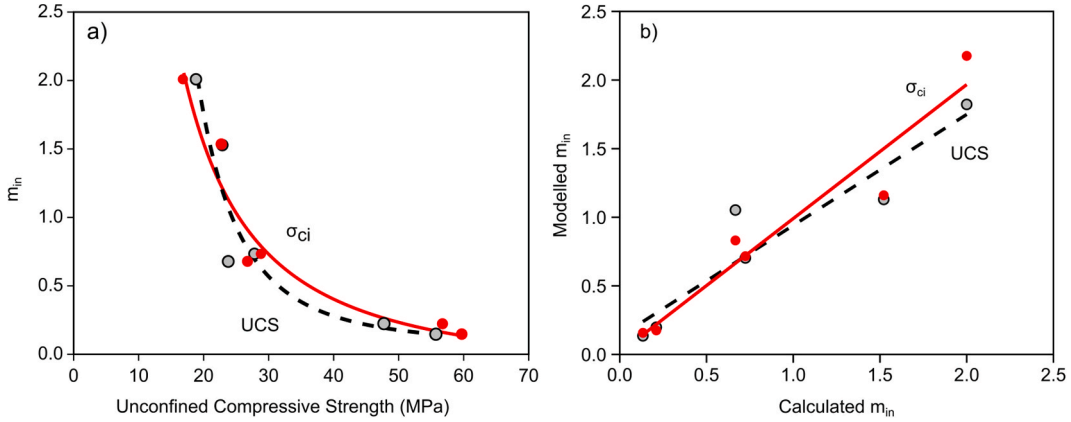

Fig. 12. Plots of a) relationship between m_{in} and UCS for m_{in} calculated with both σ_{ci} and laboratory UCS; b) calculated versus modelled m_{in} using the fitting parameters for modelled mi_n based on σ_{ci} and based on laboratory UCS.

composing the 'C' and 'D' sands of the Maui Field reservoirs (Table 7). Their aim was to establish if a relationship existed between porosity and permeability, to be able to predict permeability from porosity-derived logs. The dominant control on porosity and permeability is identified as textural grain size and grain sorting (Chantellier and Hitchings, 1987; Hill, 2020). Based on a dominant mean grain size and porosity control on rock strength, we infer that the mechanical properties of a reservoir will follow a similar spatial distribution pattern, and that stochastic models can provide the input data necessary for mechanical strength prediction. Using the two sandstone facies recognised by Chantellier and Hitchings (1987), we ascribed an average estimated UCS and Hoek Brown material constant (m_i) derived using Equations (12) and (13)

Table 7
Comparison of textural and geomechanical properties across two sandstone facies interpreted within the 'C' sands of the Maui Field. UCS is estimated using Equation (12), and m_i is estimated using Equation (13) using the empirical parameters for this dataset from Table 5.

Lithofacies	Depositional Setting	Average Porosity Fraction	Permeability (mD)	Average Grain Diameter D (μm)	Estimated UCS (MPa)	Estimated m_i
Cross-bedded Sandstones (Sx)	Channel Complexes and minor Coastal Bars	0.19	174	335	31	17
Heterolithic Sandstones (Hl)	Crevasse Splays/Overbank Deposits	0.17	33.9	161	41	12

(Table 7). This technique can be utilized for an approximate rock strength prediction across un-cored reservoir intervals. This particular example shows that the cross bedded sandstones will be weaker in comparison to the heterolithic sandstones, and that mechanical properties can be linked to facies descriptions.

6. Conclusions

- UCS of sandstone is inversely proportional to both porosity fraction and mean grain diameter. We propose an empirical relationship, that can be locally calibrated, to determine UCS as a function of both porosity fraction and grain diameter. For the purpose of this empirical relationship, grain diameter is considered independent of porosity fraction. This empirical strength relationship can be accurately extrapolated across a wide spatial and age distribution of sandstone reservoir intervals.
- The response of the Hoek-Brown and Mohr-Coulomb strength parameters to change in grain diameter suggests that these characteristics can be utilized as a predictive tool for reservoir failure in petroleum geomechanics. However, if triaxial data are not available we show that σ_{ci} can be equated with UCS, which can then be used to derive the Hoek-Brown parameter, m_i, and thus build the Hoek-Brown failure criterion for geomechanical analysis.
- This technique can be used to link facies with mechanical properties at the basin scale.
- As more UCS and triaxial data become available, these empirical relationships can continue to be calibrated to provide improved predictive tools for strength estimates and development of failure criteria for sandstone reservoirs.
- This research has provided a first analysis of dry strength results, and has been applied to published dry and saturated strength results. However more work is warranted to explore the impact of the presence of water on modelling of in-situ strength.

Credit author statement

Sophie Hill: Conceptualization, Methodology, Investigation, Formal analysis, Writing- Original draft preparation. Marlene Villeneuve: Conceptualization, Funding acquisition, Project administration, Supervision, Resources, Formal analysis, Writing- Reviewing and Editing, David McNamara: Funding acquisition, Supervision, Writing- Reviewing and Editing.

Declaration of competing interest

The authors declare that they have no known competing financial interests or personal relationships that could have appeared to influence the work reported in this paper.

Acknowledgements

This work was supported by the New Zealand Ministry of Business, Innovation and Employment (MBIE) research project "Understanding petroleum source rocks, fluids, and plumbing systems in New Zealand basins: a critical basis for future oil and gas discoveries" [grant number C05X1507]. We thank Hannu Seebeck and Karsten Kroeger for helpful comments on the manuscript, as well as six anonymous reviewers whose comments and recommendations helped refine, clarify and improve the manuscript.

Appendix A. Supplementary data

Supplementary data to this article can be found online at https://doi.org/10.1016/j.petrol.2022.110375.

References

Ashby, M.F., Sammis, C.G., 1990. The damage mechanics of brittle solids in compression. Pure Appl. Geophys. 133, 489–521. https://doi.org/10.1007/BF00878002.
ASTM International, 2014. D7012-14e1 Standard Test Methods for Compressive Strength and Elastic Moduli of Intact Rock Core Specimens under Varying States of Stress and Temperatures. ASTM International, West Conshohocken, PA.
ASTM International, 2019. D4543-19 Standard Practices for Preparing Rock Core as Cylindricl Test Specimens and Verifying Conformance to Dimensional and Shape Tolerances. ASTM International, West Conshohocken, PA.
Atapour, H., Mortazavi, A., 2018. The influence of mean grain size on unconfined compressive strength of weakly consolidated reservoir sandstones. J. Petrol. Sci. Eng. 171, 63–70.
Bal, A., Lewis, D.W., 1994. A cretaceous - early tertiary Macrotidal estuarine-fluvial succession: puponga coal measures in Whanganui inlet, onshore Pakawau sub-basin, Northwest Nelson, New Zealand. N. Z. J. Geol. Geophys. 37, 287–307.
Baud, P., Zhu, W., Wong, T.F., 2000. Failure mode and weakening effect of water on sandstone. J. Geophys. Res. Solid Earth 105, 16371–16389.
Baud, P., Louis, L., David, C., Rawlings, G.C., Wong, T.F., 2005. Effects of beddings and foliation on mechanical anisotropy and failure mode. Geol. Soc. Lond. Sp. Publ. 245, 223–249. https://doi.org/10.1144/GSL.SP.2005.245.01.11.
Baud, P., Wong, T., Zhu, W., 2014. Effects of porosity and crack density on the compressive strength of rocks. Int. J. Rock Mech. Min. Sci. 67, 202–211. https://doi.org/10.1016/j.ijrmms.2013.08.031.
Bell, F., 1978. The physical and mechanical properties of the fell sandstones, Northumberland, England. Eng. Geol. 12, 1–29.
Bésuelle, P., Baud, P., Wong, T.F., 2003. Failure mode and spatial distribution of damage in Rothbach sandstone in the brittle-ductile transition. Pure Appl. Geophys. 160, 851–868.
Browne, G.H., 2009. First New Zealand record of probable dinosaur footprints from the late Cretaceous North Cape formation, northwest nelson. N. Z. J. Geol. Geophys. 52, 367–377.
Bryant, I., Marshall, M., Greenstreet, C., Voggenreiter, W., Cohen, J., Stroemmen, J., 1994. Integrated Geological Reservoir Modelling of the Maui Field, Taranaki Basin, New Zealand. 1994 New Zealand Petroleum Conference Proceedings: the Post Maui Challenge-Investment and Development Opportunities. Energy and Resources Division, Wellington, pp. 256–281.
Carbillet, L., Heap, M.J., Baud, P., Wadsworth, F.B., Reuschlé, T., 2021. Mechanical compaction of crustal analogs made of sintered glass beads: the influence of porosity and grain size. J. Geophys. Res. Solid Earth 126 (4), e2020JB021321.
Chang, C., Zoback, M.D., Khaksar, A., 2006. Empirical relations between rock strength and physical properties in sedimentary rocks. J. Petrol. Sci. Eng. 51, 223–237.
Chantellier, J.Y., Hitchings, V.H., 1987. Geological Investigations of Cores from the C and D Reservoirs in Well Maui-7, Maui Field, New Zealand, PML 381012, New Zealand Unpublished Open File Petroleum Report 1302. Ministry of Economic Development, Wellington.
Craig, R.F., 1997. Soil Mechanics, sixth ed. E&FN Spon, ISBN 9780419224501, pp. 103–106.
Douglas, K.J., 2002. The Shear Strength of Rock Masses. University of New South Wales.
Duda, M., Renner, J., 2013. The weakening effect of water on the brittle failure strength of sandstone. Geophys. J. Int. 192 (3), 1091–1108.
Eberhardt, E., 2012. The Hoek–Brown failure criterion. Rock Mech. Rock Eng. 45 (6), 981–988. https://doi.org/10.1007/s00603-012-0276-4.
Fjaer, E., Holt, R.M., Raaen, A., Risnes, R., Horsrud, P., 2008. Petroleum Related Rock Mechanics. Elsevier.
Fredrich, J.T., Evans, B., Wong, T.F., 1990. Effect of grain size on brittle and semibrittle strength: implications for micromechanical modelling of failure in compression. J. Geophys. Res. Solid Earth 95, 10907–10920.

Folk, R.L., Andrews, P.B., Lewis, D.W., 1970. Detrital sedimentary rock classification and nomenclature for use in New Zealand. N. Z. J. Geol. Geophys. 13 (4), 937–968. https://doi.org/10.1080/00288306.1970.10418211.
Gholami, R., Moradzadeh, A., Rasouli, V., Hanachi, J., 2014. Practical application of failure criteria in determining safe mud weight windows in drilling operations. J. Rock Mech. Geotech. Eng. 6, 13–25.
Griffiths, L., Heap, M.J., Xu, T., Chen, C.F., Baud, P., 2017. The influence of pore geometry and orientation on the strength and stiffness of porous rock. J. Struct. Geol. 96, 149–160.
Heap, M.J., Farquharson, J.I., Baud, P., Lavallée, Y., Reuschlé, T., 2015. Fracture and compaction of andesite in a volcanic edifice. Bull. Volcanol. 77, 55.
Heap, M.J., Villeneuve, M., Kushnir, A.R., Farquharson, J.I., Baud, P., Reuschlé, T., 2019. Rock mass strength and elastic modulus of the Buntsandstein: an important lithostratigraphic unit for geothermal exploitation in the Upper Rhine Graben. Geothermics 77, 236–256.
Higgs, K.E., Crouch, E.M., Raine, J.I., 2017. An interdisciplinary approach to reservoir characterisation; an example from the early to middle Eocene Kaimiro Formation, Taranaki Basin, New Zealand. Mar. Petrol. Geol. 86, 111–139.
Higgs, K.E., Strogen, D., Griffin, A., Ilg, B., Arnot, M., 2012. Reservoirs of the Taranaki Basin, New Zealand. GNS Science Data Series.
Hill, S., 2020. Mechanical Rock Property Characterisation and Assessment of Sandstone Reservoirs in the Southern Taranaki Basin. PhD Thesis. University of Canterbury, New Zealand.
Hoek, E., Brown, E.T., 1980. Empirical strength criterion for rock masses. J. Geotech. Geoenviron. Eng. 106.
Hoek, E., Brown, E.T., 1997. Practical estimates of rock mass strength. Int. J. Rock Mech. Min. Sci. 34, 1165–1186.
Hoek, E., Marinos, P., 2000. Predicting tunnel squeezing problems in weak heterogeneous rock masses. Tunnels Tunn. Int. 32, 45–51.
Holt, R., Ingsoy, P., Mikkelson, M., 1989. Rock mechanical analysis of North Sea reservoir formations. SPE Form. Eval. 4, 33–37.
Joyce, R., 2018. Assessment of Paleo-Depositional Environments and Reservoir Potential of the Late Cretaceous North Cape Formation, Nelson, New Zealand. University of Canterbury, Christchurch, New Zealand.
King, P., Naish, T., Thrasher, G., 1991. Structural Cross Sections and Selected Palinspastic Reconstructions of the Taranaki Basin. New Zealand Geological Survey Report G, New Zealand, p. 150.
King, P., Thrasher, G., 1992. Post-eocene Development of the Taranaki Basin, New Zealand: Convergent Overprint of a Passive Margin: Chapter 7: Southwest Pacific and Eastern Indian Ocean Margins.
King, P.R., Thrasher, G.P., 1996. Cretaceous Cenozoic Geology and Petroleum Systems of the Taranaki Basin. Institute of Geological & Nuclear Sciences, New Zealand, p. 243 p + 6 enclosures.
Koninklijke/Shell Exploratie, 1986. Geological Investigations of Cores from the C1 and D1 Reservoirs in Well Maui A1 (G) Maui Field New Zealand. New Zealand Unpublished Open File Petroleum Report 818. Ministry of Economic Development, Wellington.
Labuz, J.F., Zang, A., 2012. Mohr–Coulomb failure criterion. Rock Mech. Rock Eng. 45, 975–979.
Martin, K.R., 2001. Petrology, Diagenesis and Reservoir Quality of Kapuni Group Sandstones in Pohokura-1 and Pohokura-2, PEP38459, Taranaki Basin. New Zealand Unpublished Open File Petroleum Report 2601. Ministry of Economic Development, Wellington.
Massiot, C., Seebeck, H., Nicol, A., Mcnamara, D.D., Lawrence, M.J., Griffin, A.G., Thrasher, G.P., O'brien, G., Viskovic, G.P.D., 2019. Effects of Regional and Local Stress Variabilities on Fault Slip Tendency in the Southern Taranaki Basin, New Zealand. Marine and Petroleum Geology.
Mcbeath, D., 1977. Gas-condensate fields of the Taranaki basin, New Zealand. N. Z. J. Geol. Geophys. 20, 99–127.
Moos, D., Zoback, M., Bailey, L., 2001. Feasibility study of the stability of openhole multilaterals, Cook Inlet, Alaska. SPE Drill. Complet. 16, 140–145.
New Zealand Overseas Petroleum Limited, 2005. Amokura-1 Advanced Core Analysis Study. New Zealand Unpublished Open-File Petroleum Report 3150. Ministry of Economic Development, Wellington.
New Zealand Petroleum & minerals, 2014. New Zealand Petroleum Basins [Online]. Available: https://www.nzpam.govt.nz/assets/Uploads/doing-business/nz-petroleum-basins-part-one.pdf ([Accessed]).
Nicol, A., Mazengarb, C., Chanier, F., Rait, G., Uruski, C., Wallace, L., 2007. Tectonic evolution of the active Hikurangi subduction margin, New Zealand, since the Oligocene. Tectonics 26.
OMV New Zealand Limited, 1998-2006. Maari Platform Geotechnical Information. New Zealand Unpublished Open-File Petroleum Report 3312. Ministry of Economic Development, Wellington.
Palchik, V., 1999. Influence of porosity and elastic modulus on uniaxial compressive strength in soft brittle porous sandstones. Rock Mech. Rock Eng. 32, 303–309.
Peng, J., Wong, L.N.Y., Teh, C.I., 2017. Influence of grain size heterogeneity on strength and microcracking behavior of crystalline rocks. J. Geophys. Res. Solid Earth 122 (2), 1054–1073.
Pilaar, W.F.H., Wakefield, L.L., 1978. Structural and stratigraphic evolution of the Taranaki basin, offshore North Island, New Zealand. APPEA J. 18, 93–101.
Ramamurthy, T., 1993. Strength and modulus responses of anisotropic rocks. Comprehen. Rock Eng. 1, 313–329.
Rawlings, J.O., Pantula, S.G., Dickey, D.A., 2001. Applied Regression Analysis: a Research Tool. Springer Science & Business Media.
Reyer, D., Philipp, S.L., 2014. Empirical relations of rock properties of outcrop and core samples from the Northwest German Basin for geothermal drilling. Geotherm. Energy Sci. 2, 21–37.
Robertson, A., 1970. Interpretation of geological factors for use in slope theory. In: Planning Open Pit Mines-Symp. On the Theoretical Background to the Planning of Open Pit Mines with Special Reference to Slope St, pp. 55–71.
Sabatakakis, N., Tsiambaos, G., Ktena, S., Bouboukas, S., 2018. The effect of microstructure on mi strength parameter variation of common rock types. Bull. Eng. Geol. Environ. 77, 1673–1688.
Sammis, C.G., Ashby, M.F., 1986. The failure of brittle porous solids under compressive stress states. Acta Metall. 34, 511–526.
Shakoor, A., Bonelli, R.E., 1991. Relationship between petrographic characteristics, engineering index properties, and mechanical properties of selected sandstones. Bull. Assoc. Eng. Geol. 28, 55–71.
Shell BP Todd Oil Services Ltd, 1976. Well Resume Tane-1 (Offshore). New Zealand Unpublished Open File Petroleum Report 698. Ministry of Economic Development, Wellington.
Shell BP Todd Oil Services Ltd, 1979. Maui Field Platform A Development Well Drilling and Completion Reports. New Zealand Unpublished Open File Petroleum Report 800. Ministry of Economic Development, Wellington.
Shell Todd Oil Services Ltd, 2001. Pohokura Field ERD Wellbore Stability Study. New Zealand Unpublished Open-File Petroleum Report 2651. Ministry of Economic Development, Wellington.
Shell Todd Oil Services Ltd, 2002. Rock Strength Measurements from Pohokura-1 and Pohokura-2. New Zealand Unpublished Open-File Petroleum Report 2778. Ministry of Economic Development, Wellington.
Shen, J., Karakus, M., 2014. Simplified method for estimating the Hoek-Brown constant for intact rocks. J. Geotech. Geoenviron. Eng. 140, 04014025.
Siratovich, P.A., Heap, M.J., Villeneuve, M.C., Cole, J.W., Kennedy, B.M., Davidson, J., Reuschlé, T., 2016. Mechanical behaviour of the Rotokawa Andesites (New Zealand): insight into permeability evolution and stress-induced behaviour in an actively utilised geothermal reservoir. Geothermics 64, 163–179.
Stos Development Department, 1993a. MB-R (1) Well Completion Report, Maui B Field. PML381012. Offshore Taranaki Basin. New Zealand Unpublished Open File Petroleum Report 1912. Ministry of Economic Development, Wellington.
Stos Development Department, 1993b. MB-W (2) Well Completion Report, Maui B Field. PML381012. Offshore Taranaki Basin. New Zealand Unpublished Open File Petroleum Report 1932. Ministry of Economic Development, Wellington.
Strogen, D.P., 2011. Updated Paleogeographic Maps for the Taranaki Basin and Surrounds. *Lower Hutt*. GNS Science, New Zealand.
Strogen, D.P., Seebeck, H., Nicol, A., King, P.R., 2017. Two-phase cretaceous–paleocene rifting in the Taranaki basin region, New Zealand; implications for gondwana break-up. J. Geol. Soc. 174, 929–946.
Swift Energy, 2007a. Geomechanical Analysis and Wellbore Stability Study of the Goss & Trapper Wells, Tawn Trend NZ. New Zealand Unpublished Open-File Petroleum Report 3751. Ministry of Economic Development, Wellington.
Swift Energy, 2007b. Geomechanical Modelling, Fracture Permeability and Drilling Options Analysis of the Kauri Field NZ. New Zealand Unpublished Open-File Petroleum Report 3752. Ministry of Economic Development, Wellington.
Sykes, R., Dow, M.J., 2000. Petroleum Source Rock Potential of North Cape Formation (Late Cretaceous) Coaly Sediments, Taranaki Basin. 2000 New Zealand Petroleum Conference Proceedings. Ministry of Commerce, Wellington, pp. 264–286.
Sykes, R., Raine, J.I., 2008. Organofacies controls on the oil potential of coaly source rocks in the Late Cretaceous North Cape Formation. Taranaki Basin.
Tang, S.B., Yu, C.Y., Heap, M.J., Chen, P.Z., Ren, Y.G., 2018. The influence of water saturation on the short-and long-term mechanical behavior of red sandstone. Rock Mech. Rock Eng. 51 (9), 2669–2687.
Thrasher, G.P., 1990. Tectonics of the Taranaki Rift. *1989 New Zealand Petroleum Conference Proceedings*. Wellington, New Zealand: Petroleum and Geothermal Unit, Energy and Resources Division. Ministry of Commerce.
Thrasher, G.P., 1992. Last Cretaceous Geology of Taranaki Basin. University of Canterbury, New Zealand (Christchurch, New Zealand).
Titheridge, D.G., 1977. Stratigraphy and Sedimentology of the Upper Pakawau and Lower Westhaven Groups.
Todd Energy, 2010. Te Kiri Prospect Geomechanical Analysis. PEP51149. New Zealand Unpublished Open-File Petroleum Report 4278. Ministry of Economic Development, Wellington.
Tricentrol Exploration Overseas Ltd., 1984. Well Completion Report Moki-1. Petroleum Report Series PR987. Ministry of Economic Development.
Ulusay, R., Hudson, J.A., 2007. The Complete ISRM Suggested Methods for Rock Characterization, Testing and Monitoring. ISRM Turkish National Group, Ankara, Turkey.
Ulusay, R., Türeli, K., Ider, M.H., 1994. Prediction of engineering properties of a selected litharenite sandstone from its petrographic characteristics using correlation and multivariate statistical techniques. Eng. Geol. 38, 135–157.
Vásárhelyi, B., Kovács, L., Török, Á., 2016. Analysing the modified Hoek–Brown failure criteria using Hungarian granitic rocks. Geomech. Geophys. Geo Energy Geo Resour. 2, 131–136.
Vernik, L., Bruno, M., Bovberg, C., 1993. Empirical Relations between Compressive Strength and Porosity of Siliciclastic Rocks. International Journal of Rock Mechanics and Mining Sciences & Geomechanics Abstracts. Elsevier, pp. 677–680.
Villeneuve, M.C., Heap, M.J., Kushnir, A., Qin, T., Baud, P., Zhou, G., Xu, T., 2018. Estimating in situ rock mass strength and elastic modulus of granite from the Soultz-sous-Forêts geothermal reservoir (France). Geoth. Energy 6, 11.

Villeneuve, M.C., Heap, M.J., 2021. Calculating the cohesion and internal friction angle of volcanic rocks and rock masses. Volcanica 4, 279–293. https://doi.org/10.30909/vol.04.02.279293.
Wasantha, P.L., Ranjith, P.G., 2014. Water-weakening behavior of Hawkesbury sandstone in brittle regime. Eng. Geol. 178, 91–101.
Wong, R.H.C., Chau, K.T., Wang, P., 1996. Microcracking and grain size effect in Yuen Long marbles. In: International *Journal of Rock Mechanics and Mining Sciences & Geomechanics Abstracts*. Elsevier, pp. 479–485.
Wong, T.F., David, C., Zhu, W., 1997. The transition from brittle faulting to cataclastic flow in porous sandstones: mechanical deformation. J. Geophys. Res. Solid Earth 102, 3009–3025.
Xu, T., Fu, T.F., Heap, M.J., Meredith, P.G., Mitchell, T.M., Baud, P., 2020. Mesoscopic damage and fracturing of heterogeneous brittle rocks based on three-dimensional polycrystalline discrete element method. Rock Mech. Rock Eng. 53 (12), 5389–5409.
Yu, Q., Zhu, W., Ranjith, P.G., Shao, S., 2018. Numerical simulation and interpretation of the grain size effect on rock strength. Geomech. Geophys. Geo Energy Geo Resour. 4 (2), 157–173.
Zhang, J., Rai, C.S., Sondergeld, C.H., 1998. Mechanical strength of reservoir materials: key information for sand prediction. SPE ISRM Rock Mech. Petrol. Eng.
Zhang, L., Cao, P., Radha, K., 2010. Evaluation of rock strength criteria for wellbore stability analysis. Int. J. Rock Mech. Min. Sci. 47, 1304–1316.
Zoback, M.D., 2010. Reservoir Geomechanics. Cambridge University Press.